

Enhanced-resolution using modified configuration of Fresnel incoherent holographic recorder with synthetic aperture

Yuval Kashter* and Joseph Rosen

Department of Electrical and Computer Engineering, Ben-Gurion University of the Negev, P.O. Box 653, Beer-Sheva 8410501, Israel

*kashter@ee.bgu.ac.il

Abstract: Synthetic aperture methods are commonly-used techniques for providing images with super-resolution qualities. We propose an improved design of the system, coined “synthetic aperture with Fresnel elements”. The super-resolution capabilities of the proposed scheme are analyzed and experimentally demonstrated.

©2014 Optical Society of America

OCIS codes: (090.0090) Holography; (280.6730) Synthetic aperture radar; (110.6770) Telescopes; (050.1965) Diffractive lenses; (050.5080) Phase shift; (090.1760) Computer holography; (090.2890) Holographic optical elements; (110.3175) Interferometric imaging.

References and links

1. E. Abbe, “Beiträge zur Theorie des Mikroskops und der mikroskopischen Wahrnehmung,” *Archiv. Mikroskopische Anat.* **9**(1), 413–418 (1873).
2. A. A. Michelson, “On the application of interference methods to astronomical measurements,” *Proc. Natl. Acad. Sci. U.S.A.* **6**(8), 474–475 (1920).
3. P. R. Lawson, *Selected Paper on Long Baseline Stellar Interferometry*, (SPIE Press Book, 1997).
4. M. E. Testorf and M. A. Fiddy, “Superresolution imaging-revisited,” *Adv. Imaging Electron Phys.* **163**, 165–218 (2010).
5. S. M. Beck, J. R. Buck, W. F. Buell, R. P. Dickinson, D. A. Kozłowski, N. J. Marechal, and T. J. Wright, “Synthetic-aperture imaging laser radar: laboratory demonstration and signal processing,” *Appl. Opt.* **44**(35), 7621–7629 (2005).
6. V. Micó, Z. Zalevsky, P. García-Martínez, and J. García, “Synthetic aperture superresolution with multiple off-axis holograms,” *J. Opt. Soc. Am. A* **23**(12), 3162–3170 (2006).
7. L. Granero, V. Micó, Z. Zalevsky, and J. García, “Synthetic aperture superresolved microscopy in digital lensless Fourier holography by time and angular multiplexing of the object information,” *Appl. Opt.* **49**(5), 845–857 (2010).
8. L. Martínez-León and B. Javidi, “Synthetic aperture single-exposure on-axis digital holography,” *Opt. Express* **16**(1), 161–169 (2008).
9. K. Ji, P. Gao, J. Min, R. Guo, and N. Menke, “A synthetic aperture telescope based on a pair of gratings,” *J. Mod. Opt.* **60**(15), 1229–1233 (2013).
10. G. Indebetouw, Y. Tada, J. Rosen, and G. Brooker, “Scanning holographic microscopy with resolution exceeding the Rayleigh limit of the objective by superposition of off-axis holograms,” *Appl. Opt.* **46**(6), 993–1000 (2007).
11. J. Rosen and G. Brooker, “Digital spatially incoherent Fresnel holography,” *Opt. Lett.* **32**(8), 912–914 (2007).
12. J. Rosen and G. Brooker, “Non-Scanning Motionless Fluorescence Three-Dimensional Holographic Microscopy,” *Nat. Photonics* **2**(3), 190–195 (2008).
13. P. Bouchal, J. Kapitán, R. Chmelík, and Z. Bouchal, “Point spread function and two-point resolution in Fresnel incoherent correlation holography,” *Opt. Express* **19**(16), 15603–15620 (2011).
14. J. Rosen, N. Siegel, and G. Brooker, “Theoretical and experimental demonstration of resolution beyond the Rayleigh limit by FINCH fluorescence microscopic imaging,” *Opt. Express* **19**(27), 26249–26268 (2011).
15. B. Katz, J. Rosen, R. Kelner, and G. Brooker, “Enhanced resolution and throughput of Fresnel incoherent correlation holography (FINCH) using dual diffractive lenses on a spatial light modulator (SLM),” *Opt. Express* **20**(8), 9109–9121 (2012).
16. B. Katz and J. Rosen, “Super-resolution in incoherent optical imaging using synthetic aperture with Fresnel elements,” *Opt. Express* **18**(2), 962–972 (2010).
17. B. Katz and J. Rosen, “Could SAFE concept be applied for designing a new synthetic aperture telescope?” *Opt. Express* **19**(6), 4924–4936 (2011).

18. G. Brooker, N. Siegel, V. Wang, and J. Rosen, "Optimal resolution in Fresnel incoherent correlation holographic fluorescence microscopy," *Opt. Express* **19**(6), 5047–5062 (2011).
 19. J. W. Goodman, *Introduction to Fourier optics, 3rd Ed.*, (Roberts and Company Publishers, 2005).
 20. X. Lai, S. Zeng, X. Lv, J. Yuan, and L. Fu, "Violation of the Lagrange invariant in an optical imaging system," *Opt. Lett.* **38**(11), 1896–1898 (2013).
-

1. Introduction

It is well established that the resolving power of an imaging system is limited by the wave nature of light [1]. The ability to exceed the resolving power beyond the diffraction limits is a widely studied topic among many research groups [2–9]. A common approach to achieving this goal is by forming a synthetic aperture (SA). According to this method, several interference patterns are captured by an aperture-limited system (i.e., a system limited by its physical aperture) from various points of view. These interferograms are tiled into a new larger pattern, which could be considered to be formed by a virtual equivalent imaging system with a much wider aperture [2, 3, 5–9]. This approach enlarges the effective aperture of the system, which is now equivalent to an imaging system with a higher numerical aperture (NA) value. Therefore, SA is considered to be a super-resolution technique, as it provides resolutions that exceed the theoretical limit dictated by the system's physical aperture [4].

Methods of SA are frequently implemented by holographic imaging. However, these are usually restricted to coherent imaging [5–8] and thus are limited to applications in which the observed target can be illuminated by lasers. An SA system that uses incoherent scanning holography was introduced by Indebetouw *et al.* [10], but has been limited to microscopy. Although the method is based on incoherent holograms, the specimen should also be illuminated by an interference pattern obtained from two laser beams. A recent innovation, called Fresnel incoherent correlation holography (FINCH) enables three-dimensional (3D) holographic imaging of objects without coherent laser illumination [11, 12]. In FINCH, shown in Fig. 1(a), spherical beams of light are reflected or emitted from every point source located on a 3D object. Each beam, while propagating through the system, is modified by a phase-only spatial light modulator (SLM), employed as a diffractive beam splitter of the incoherent interferometer. Consequently, each beam of light is split into two spherical waves of different curve radii. The two waves interfere on the camera plane, where their interferogram encodes the 3D location and intensity value of each point source. Summing the interferograms of the total spherical beam couples creates a Fresnel hologram of the entire observed 3D scene [11–13]. Thus, in FINCH, the object itself serves as the only light source for each of the interfered waves and, therefore, no external active coherent illumination (i.e., laser beam) is needed.

The early studies of FINCH [11–13] presented a method of interfering between plane and spherical waves. Later on [14, 15], it was demonstrated, theoretically and experimentally, that the imaging resolution of FINCH is beyond the Rayleigh resolution limit when compared to conventional incoherent and coherent imaging systems with the same NA. Furthermore, it was demonstrated [15] that interfering between two closely spaced spherical waves, instead of a plane and a spherical wave, provides FINCH which can operate with a wider bandwidth of light and without any resolution loss, as long as the two interfering beams from any source point perfectly overlap on the camera plane. Using two closely spaced spherical waves reduces the maximal optical path difference (OPD) between the two interfering waves, resulting in higher quality of the recorded holograms.

In a recent study, a new type of incoherent holographic FINCH-based system, dubbed SA with Fresnel element (SAFE) [16], has been proposed. This holographic system creates an SA by combining several Fresnel sub-holograms captured from various viewpoints by a system with a limited physical aperture. The system contains a band pass filter (BPF), a polarizer, an SLM and a digital camera. The SA is implemented by shifting the BPF-polarized-SLM-camera set along several viewpoints (see Fig. 1 in Ref [16]). At each viewpoint, a different mask is displayed on the SLM with respect to the system's position and a single element of

the Fresnel hologram is recorded. The various elements are tiled together to form a final mosaic hologram, which is considered to have been captured from a single SA that is much wider than the physical aperture.

More recently, another scheme of SAFE has been proposed, dubbed telescopic SAFE (T-SAFE) [17]. In T-SAFE, due to a modification of the original SAFE setup, the resolution is improved by the ratio between the synthetic and the physical aperture widths. This result is achieved by choosing the optimal (in the sense of best resolution) focal length of the diffractive lens displayed on the SLM. SAFE and T-SAFE do, indeed, improve the resolution performance beyond the Rayleigh limit. However, in both cases the interference occurs between plane and spherical waves and thus the maximal OPD between the waves is relatively long. Furthermore, the process of tiling the sub-holograms together demands complicated image processing. Additionally, T-SAFE was only demonstrated on a simple object of two uncorrelated point sources using two independent HeNe lasers, while the SA was implemented only along the horizontal axis.

In this study we propose a new approach for achieving an SA, inspired by the SAFE and T-SAFE concepts, as follows:

- We propose an SA system in which for every object point, the interference occurs between two closely spaced spherical waves with different curve radii, rather than between spherical and plane waves, as in Refs [16, 17]. The system configuration fulfills the requirement of overlap between the two waves on the camera plane, and thus the optimal resolution condition is satisfied. Therefore, the maximal OPD between the two interfered waves is shorter than that of the T-SAFE system, without sacrificing the system resolution.
- Similarly to T-SAFE, multiple Fresnel sub-holograms are tiled together to form a new large hologram. However, in contrast to the T-SAFE scheme, in order to prevent distorted images, the stitches between the sub-holograms never pass through the center of the mosaic hologram.
- We demonstrate the super-resolution capabilities of the system on a full two-dimensional (2D) plane. The tested object is more complicated than in previous studies, as it is a segment of resolution chart (RC) containing symbols, horizontal and vertical equally-spaced parallel bars, illuminated by spatially incoherent light.
- We present a simple and accurate method of tiling the sub-holograms into the large synthetic hologram.

2. Method and analysis of dual lens SAFE

In the following section we describe the modified SAFE system and analyze its performance. In order to achieve the best reconstructed image with minimum distortions, the stitch between sub-holograms should not pass through the center of the mosaic hologram. This is because a major amount of intensity emitted from test objects propagates toward the system in a relatively small angular aperture and thus any discontinuity through the area of most of the light might distort the reconstructed image. Hence, in the present study, a continuous central sub-hologram is recorded by a conventional dual lens FINCH [14, 15] system. The central incoherent sub-hologram of an object point located on the front focal plane of a collimating lens L_1 , with the transverse position of $\vec{r}_s = [x_s, y_s]$, is created in a single-channel system by the interference between two spherical waves converging to the distances f_1 and f_2 from the SLM (See Fig. 1(a)). The collimation lens L_1 converts the spherical wave emitted from the object point into a plane wave at the entrance of the system. Thus, the lens L_1 is employed here as an imager for objects located at infinity and, therefore, it is not considered as part of the holographic system. According to Ref [18], for maximum visibility of the interference

between the two waves, two polarizers P_1, P_2 , oriented at 45° with respect to the SLM active axis, are positioned before and after the SLM. An additional glass lens L_2 is used to convert the plane wave obtained from L_1 into a converging spherical wave, which is then split by the SLM into two spherical waves. As mentioned above, in order to achieve optimal resolution with dual lens FINCH, the two spherical interfering beams should overlap on the camera plane. To fulfill this requirement, the distance between the SLM and the camera plane z_h should be [14, 15]

$$z_h = \frac{2f_1f_2}{f_1 + f_2}. \quad (1)$$

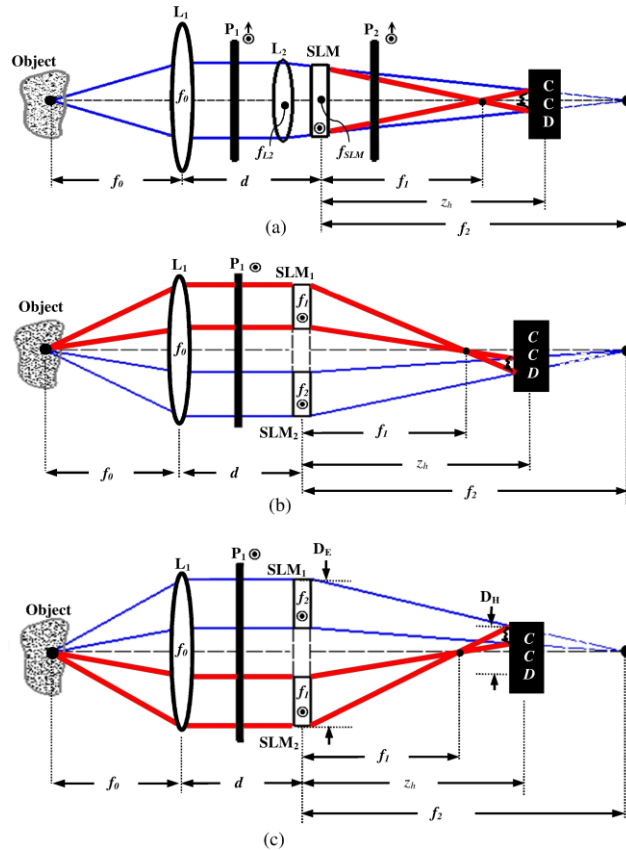


Fig. 1. Schematic configurations of the dual lens SAFE concept: L_1 and L_2 , lenses; P_1 and P_2 , polarizers; SLM, SLM_1 and SLM_2 , spatial light modulators; CCD, charged couple device. These elements create (a) a continuous central holographic element by implementing a dual lens FINCH method, f_{SLM} is the focal length of the diffractive lens displayed on the SLM and f_{L2} is the focal length of the glass lens L_2 , (b) a marginal holographic element, where SLM_1 and SLM_2 are shifted in two symmetrical viewpoints in front of the collimation lens L_1 ; two diffractive lenses with focal lengths f_1 and f_2 are displayed on SLM_1 and SLM_2 , respectively and (c) similar to (b), but the diffractive lenses f_1 and f_2 are switched. D_E , D_H are the synthetic aperture and the total digital hologram width, respectively. The symbols \odot and \otimes represent polarization directions, perpendicular and 45° with respect to the plane of the page, respectively.

In the next step, the SA is implemented by shifting two SLMs, denoted SLM₁ and SLM₂, in opposite directions away from the center. Similarly to the T-SAFE [17] method, the two peripheral parts of the spherical wave emitted from the object point are directed by the two SLMs to interfere on the camera plane, enabling an additional sub-hologram to be recorded. However, in this study, contrary to T-SAFE, two converging spherical waves are created by SLM₁ and SLM₂. The diffractive element creating the two tilted converging spherical waves is composed of two different segments of quadratic phase functions, one with focal length f_1 and the other with focal length f_2 , displayed on SLM₁ and SLM₂, respectively (Figs. 2(b) and 2(c)). The two SLMs are positioned symmetrically on two opposite sides of the optical axis, as shown in Figs. 1(b) and 1(c). This configuration creates interference between two different spherical waves, propagating in two different channels, while the distance z_h is kept identical at the value given by Eq. (1). The additional lens L₂ is no longer necessary, since the two different channels have been separated. In order to achieve maximal power efficiency, the exit polarizer P₂ is removed, while the entrance polarizer P₁ is adjusted to the same orientation of the active axis of the SLMs.

Switching between the two masks, whereas SLM₁ and SLM₂ remain at the same positions mentioned above, creates a symmetrical Fresnel holographic element on the opposite side of the optical axis [Fig. 1(c)]. Thus, at every position of the SLMs (besides the central position), the system records two sub-holograms, where the partial quadratic phase functions with focal lengths f_1 and f_2 firstly, and then f_2 and f_1 secondly, are displayed on SLM₁ and SLM₂, respectively.

A mathematical analysis of the proposed system, based on the Fresnel propagation formula in the paraxial approximation [19], is hereby provided. Consider an object composed of spatially incoherent point sources, each emitting a quasi-monochromatic spherical wave. This system can be characterized by its point spread function (PSF). The complex amplitude induced just before the lens L₁ of every object point, located at $(x_s, y_s, -f_0)$ with a complex amplitude of $\sqrt{I_s}$, is expressed as $\sqrt{I_s}C(\bar{r}_s)L(-\bar{r}_s)Q(1/f_0)$, where f_0 is the focal length of the lens L₁, Q designates the quadratic phase function of the form: $Q(b) = \exp\left[i\pi b\lambda^{-1}(x^2 + y^2)\right]$, λ is the central wavelength of the light source, L denotes the linear phase function of the form: $L(\bar{s}) = \exp\left[i2\pi\lambda^{-1}(s_x x + s_y y)\right]$, and $C(\bar{r}_s)$ is a complex constant dependent on the location of the point source. For the sake of simplification, we assume that the axial distance between the lens L₂ and the SLM is negligible. As the plane wave meets a single SLM for the central sub-hologram (Fig. 1(a)), or two SLMs for the marginal sub-holograms [Figs. 1(b) and 1(c)], the wave is split into two truncated spherical waves modulated by two different quadratic phase elements. Thus, the input complex amplitude in the (m, n) th exposure is multiplied by the function $P_{mm}(x, y; \theta)$, given by

$$P_{mm}(x, y; \theta) = C_1 Q\left(\frac{-1}{f_1}\right) \text{rect}\left(\frac{x - A_x \cdot m}{A_x}, \frac{y - A_y \cdot n}{A_y}\right) + C_2 Q\left(\frac{-1}{f_2}\right) \exp(i\theta) \text{rect}\left(\frac{x + A_x \cdot m}{A_x}, \frac{y + A_y \cdot n}{A_y}\right), \quad (2)$$

where f_1 and f_2 are real constants representing the focal distances of the two converging spherical waves (relative to the SLM plane), C_1 and C_2 are constants, θ is one of the three angles used in phase shifting in order to eliminate the twin image and the bias terms from the final hologram, in accordance with Refs [11–15]. The limiting function of each physical aperture is a rectangular function defined by

$$\text{rect}\left(\frac{x}{\alpha}, \frac{y}{\beta}\right) \equiv \begin{cases} 1 & (|x|, |y|) \leq (\alpha/2, \beta/2) \\ 0 & \text{otherwise} \end{cases}.$$

In the case of $m = n = 0$, a single central mask consisting of a diffractive lens with a focal length of $f_{SLM} = f_2 f_1 / (f_2 - f_1)$ (according to the formula of chaining thin lenses) is displayed on a single SLM (Fig. 2(a)), yielding the central sub-hologram. Otherwise, a pair of two symmetrical masks consisting of two diffractive lenses with focal lengths f_1 and f_2 is displayed on SLM₁ and SLM₂, respectively. For example, $m = -n = \pm 1$ corresponds to two symmetrical marginal holographic elements along the diagonal, as is shown in Fig. 2(b) and 2(c).

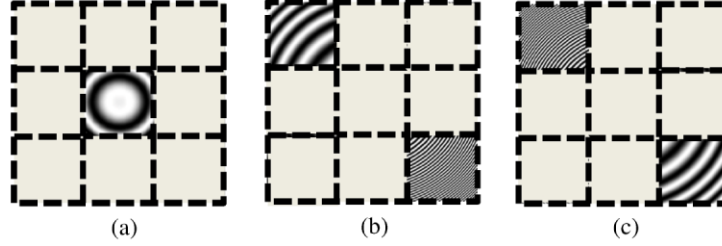


Fig. 2. (a) In the case of $m = n = 0$, the central mask consists of diffractive lens with a focal length of f_{SLM} . (b) In the case of $m = -n = 1$, two masks consisting of two diffractive lenses with focal lengths of f_1 and f_2 are shifted from the center by a distance of $(A_x, -A_y)$ and $(-A_x, A_y)$, respectively. (c) In the case of $m = -n = -1$, two masks consisting of two diffractive lenses with focal lengths of f_2 and f_1 are shifted from the center by a distance of $(-A_x, A_y)$ and $(A_x, -A_y)$, respectively.

Beyond the SLM plane, there are two waves propagating in free space over an additional distance along z_h . Thus, under the Fresnel approximation, the complex amplitude is convolved with the function $Q(1/z_h)$. Finally, the magnitude of the interference pattern is squared in order to yield the intensity distribution, which is recorded by the CCD. Hence, a complete Fresnel hologram of the object point located at $(x_s, y_s, -f_0)$ is given as a sum of $M \times N$ sub-holograms, as follows:

$$I(\bar{r}_0; \bar{r}_s) = \sum_{m=\frac{1-M}{2}}^{\frac{M-1}{2}} \sum_{n=\frac{1-N}{2}}^{\frac{N-1}{2}} \left| \sqrt{I_s} C(\bar{r}_s) L(-\bar{r}_s) Q\left(\frac{1}{f_0}\right) Q\left(-\frac{1}{f_0}\right) * Q\left(\frac{1}{d}\right) \right. \\ \left. \times P_{mn}(x, y; \theta) * Q\left(\frac{1}{z_h}\right) \right|^2, \quad (3)$$

where the asterisk denotes a 2D convolution, $\bar{r}_0 = (x_0, y_0)$ is the location vector of the CCD plane, M and N are assumed to be odd numbers, and $P_{mn}(x, y; \theta)$ is given by Eq. (2). In order to eliminate the twin image and the bias term, in every (m, n) th position three holograms are recorded and superimposed with three different values of θ [11–15]. Following previous calculations presented in [16], Eq. (3) can be written in the form of:

$$I(\bar{r}_0; \bar{r}_s) = \left(C_3 + C_4(\bar{r}_s) \mathcal{Q}\left(-\frac{1}{z_r}\right) \mathcal{L}(-\bar{r}_r) \exp(-j\theta) + C_4^*(\bar{r}_s) \mathcal{Q}\left(\frac{1}{z_r}\right) \mathcal{L}(\bar{r}_r) \exp(j\theta) \right) \times \sum_{m=\frac{1-M}{2}}^{\frac{M-1}{2}} \sum_{n=\frac{1-N}{2}}^{\frac{N-1}{2}} \text{rect}\left(\frac{x-A_x \cdot m}{A_x}, \frac{y-A_y \cdot n}{A_y}\right), \quad (4)$$

where C_3 and C_4 are constants and z_r is the reconstruction distance from the hologram (CCD plane) to the reconstructed image point, given by

$$z_r = \pm \frac{(z_h - f_1)(f_2 - z_h)}{f_2 - f_1}. \quad (5)$$

The \pm indicates that there are two possible reconstructed images, although only one of them is chosen to be the reconstruction distance, as desired. The vector $\bar{r}_r = (x_r, y_r)$ is the transversal location of the reconstructed image point, given by

$$\bar{r}_r = (x_r, y_r) = \left(\frac{x_s z_h}{f_0}, \frac{y_s z_h}{f_0} \right). \quad (6)$$

Equation (4) expresses the transparency function of a Fresnel hologram created by an object point that was recorded by an equivalent dual lens FINCH with a synthetic aperture of the size $M \times A_x \times N \times A_y$. The transverse magnification is expressed as $M_T = \partial x_r / \partial x_s = z_h / f_0$ and is the same as the magnification of the conventional dual lens FINCH [15]. Assuming that the mosaic hologram is a rectangle of dimension $D_H \times D_H$, the first zero of the PSF in the object plane, which dictates the resolution limit, is

$$\Delta_0 = \frac{\lambda}{2M_T NA_{out}} = \frac{\lambda |z_r|}{M_T D_H}, \quad (7)$$

where NA_{in} and NA_{out} are the numerical apertures of the input and output complete holographic system, respectively. In practice the NA at the entrance is dictated by the diameter of the collimation lens L_I and its focal length f_0 . However, in our case, the entrance of the holographic system is defined as the plane of the SLM and, therefore, NA_{in} is considered to be $NA_{in} = D_E / 2f_0$, where D_E is the total effective SA. D_H is the width of the digital hologram; hence NA_{out} is determined by D_H and z_r . However, based on Ref [15], in the case where a perfect overlap is obtained between the two interfering beams (Eq. (1) is fulfilled), the product $NA_{out} M_T$ in FINCH is greater than NA_{in} . Therefore, the first PSF zero in a regular imaging system ($\Delta_0 = \lambda / 2NA_{in}$) is larger than in FINCH ($\Delta_0 = \lambda / 2M_T NA_{out}$).

A different approach to analyzing the FINCH resolution is via the violation of the Lagrange invariant, as was indicated by Refs [13,20]. Any conventional imaging system in homogeneous space satisfies the condition $M_T = NA_{in} / NA_{out}$, which is known as a form of the Lagrange invariant. However, in general, the Lagrange invariant is violated in FINCH and, specifically, whenever there is an overlap between the two spherical waves on the camera plane, the condition $M_T = 2NA_{in} / NA_{out}$ is satisfied. Therefore, the resolution of FINCH is inherently better than that of conventional imaging systems.

From Fig. 2(c) it is easy to see that the value of D_H is

$$D_H = \frac{D_E(f_2 - z_h)}{f_2}. \quad (8)$$

Substituting Eqs. (1), (5) and (8) into Eq. (7) yields that the PSF first zero is:

$$\Delta_0 = \lambda / 4NA_{in} \quad (9)$$

As mentioned above, Eq. (4) describes the PSF of the system for recording a Fresnel hologram. Thus, the complete Fresnel hologram of a general object with an intensity distribution of $I_s(x_s, y_s)$, illuminated by an incoherent and quasi-monochromatic light source, is an integral of the entire PSF given by Eq. (4) over all the object intensity distribution, as follows:

$$H(\bar{r}_0) = I_s(\bar{r}_s) * I(\bar{r}_0; \bar{r}_s). \quad (10)$$

In conclusion, the mosaic hologram given in Eq. (10) is a Fresnel hologram, with an effective aperture of size $M \times A_x \times N \times A_y$.

In order to calibrate the system, several sub-holograms of a single object point are first recorded from several points of views. Each sub-hologram, when reconstructed, yields a low-resolved image of the source. Next, all the sub-holograms are tiled together to one big mosaic hologram, according to the original points of view from which these sub-holograms have been captured. However, the exact position of each sub-hologram is determined according to the rule that the entire reconstructed image points should overlap, such that the reconstruction of the complete mosaic hologram is a single sharp image point. The final positions of the entire sub-holograms are memorized and are used to locate the next set of recorded sub-holograms, but this time for a more complicated object. This method, coined the True Position Calibration Technique (TPCT) provides the ability to tile the sub-holograms in a simple and accurate way.

3. Experiments and Results

3.1 Experimental methods

The dual lens SAFE concept was tested by implementing the proposed system described in section 2 and the schemes of Fig. 1. The experimental setups are illustrated in Figs. 3(a) and 3(b), where two types of objects have been tested. The first object is a single point source, which is implemented with a pinhole illuminated by a HeNe laser ($\lambda = 631nm$). The second object is a segment of an amplitude-type transmission RC, NBS 1963A, illuminated with a LED (Thorlabs LED631E, 4mW, $\lambda = 631nm$, $\Delta\lambda = 10nm$). In order to demonstrate the shifts of SLM₁ and SLM₂, suggested in Figs. 1(b) and 1(c), nine squares of 360×360 pixels ($A_x = A_y = 360$) were allocated, according to Fig. 2, on a single Holoeye PLUTO SLM (1920 \times 1080 pixels, 8 μ m pixel pitch, phase only modulation). The SA system is composed of nine physical apertures of $2.88 \times 2.88mm$ each; all of them are displayed on a single SLM. This partition makes it possible to increase the dimension of the physical aperture by a factor of three in every direction and, as a result, an SA of $8.64 \times 8.64mm$ or 1080×1080 pixels is obtained. Thus, different positions of the two SLMs are achieved without any mechanical movements. Consequently, the experimental procedure is simplified and the concept is demonstrated while using only a single SLM.

In order to achieve the best results with the given source bandwidth, the maximum OPD between the two channels should be considered. According to Ref [15], the maximum OPD is $D_E^2 \Delta f / 4f_1 f_2$, where $\Delta f = |f_2 - f_1|$. This maximum OPD should be smaller than the coherence length of the light source, which is approximately the ratio $\lambda^2 / \Delta\lambda$, where $\Delta\lambda$ and λ are the bandwidth and the central wavelength of the light source, respectively. For the

experimental values of $\lambda = 631nm$, $\Delta\lambda = 10nm$, $D_E = 8.64mm$, $f_1 = 381.6mm$ and $f_2 = 945mm$, the value of Δf must not exceed $767mm$. Hence, the focal difference $\Delta f = 563.4mm$ of the system is beneath the upper limit mentioned above. Additionally, we chose lenses L_1 and L_2 to be glass bi-convex spherical lenses with aperture diameters of $25.4mm$, where the focal lengths are $f_{o1} = 400mm$ and $f_{L2} = 1000mm$, respectively.

In the first stage, the central sub-hologram was recorded with a regular dual lens FINCH setup, as illustrated in Fig. 3(a). On the SLM, a central phase mask of a quadratic phase function (consisting of 360×360 pixels) with a focal length of $f_{SLM} = 640mm$ was displayed. The two polarizers P_1 and P_2 , rotated by 45° with respect to the active axis of the SLM, were added to the setup. Three holograms were recorded in order to eliminate the twin image and the bias term mentioned previously.

Next, the eight marginal Fresnel sub-holograms were recorded using the setup illustrated in Fig. 3(b). In this configuration, the lens L_2 and the polarizer P_2 were removed and the polarizer P_1 was rotated to be collinear with the active axis of the SLM. In order to implement the shifted pairs of apertures (as presented in Figs. 1(b) and 1(c)), we displayed two sub-masks on the SLM along four directions with the appropriate partial quadric phase functions. The sub-masks, displayed on SLM_1 and SLM_2 , had focal lengths of f_1 and f_2 , respectively, where the amount of shift was ± 360 pixels in all directions from the center. Figure 4(g) presents the nine combinations of the sub-masks displayed on the SLM.

To compare SAFE with other imaging systems, we used the same arrangement (positions of the CCD, SLM, glass lenses, etc.) to implement a conventional imaging system with an aperture of 2.88×2.88 mm (360×360 pixels), as illustrated in Fig. 3(c), and a dual lens FINCH with an aperture of 8.64×8.64 mm (1080×1080 pixels), as illustrated in Fig. 3(d). These additional setups enable us to compare dual lens SAFE with equivalent systems in order to analyze its capabilities and limitations, as described in detail below.

The nine obtained Fresnel holographic elements were tiled by implementing the TPCT mentioned in section 2, where the central holographic element has been assigned to be the reference element. Thus, at first, the central element was reconstructed by Fresnel back propagation; within its reconstructed image, the position of the pixel with the maximal intensity value was located. Afterwards, the eight marginal elements were reconstructed in the same way and for every reconstruction the pixel with the maximal intensity value was located. Later on, the distances between the reconstructed points and the reference point were measured. These measured values are defined as $\delta x_i, \delta y_i$, where i represents the indexing of the eight marginal elements ($i = 1, 2, \dots, 8$). Every i_{th} marginal element was shifted by a distance of $-\delta x_i, -\delta y_i$. Finally, the complete mosaic Fresnel hologram was generated (Fig. 4(h)).

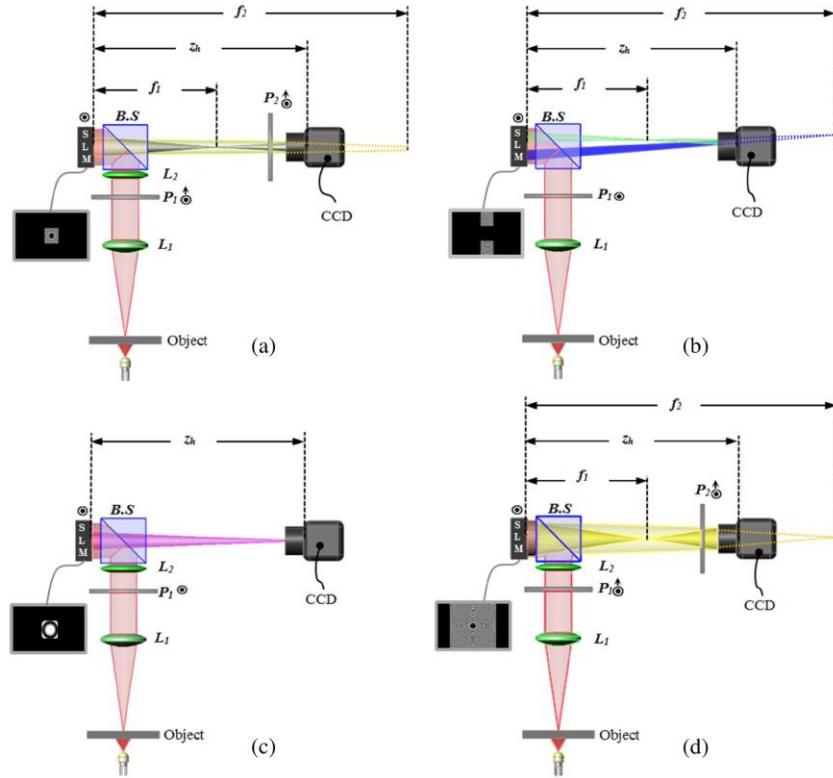


Fig. 3. Experimental setups: L_1 and L_2 , lenses; P_1 and P_2 , polarizers; SLM, spatial light modulator; CCD, charged couple device; BS, beam splitter. (a) Configuration for the central holographic element, (b) configuration for the marginal holographic elements, (c) configuration of a conventional imaging system with aperture of 360×360 pixels, (d) configuration of dual lens FINCH with aperture of 1080×1080 pixels.

3.2 PSF results

In the first experiment, we recorded a hologram of a single point source using the dual lens SAFE model, implemented by the setups illustrated in Figs. 3(a) and 3(b), in order to analyze the system's PSF. Moreover, synthesizing a hologram of a point source enables to implement the TPCT discussed above. In this section, we compare the experimental results obtained by the hologram reconstruction with those obtained by a regular dual lens FINCH, with a physical aperture of 360×360 pixels ($2.88 \times 2.88 \text{ mm}$). The purpose of this comparison is to estimate the SA resolution capabilities. Additionally, the results are compared with those of FINCH, with a physical aperture of 1080×1080 pixels ($8.64 \times 8.64 \text{ mm}$), implemented by the setup illustrated in Fig. 3(d), which is equal to the size of the SA in this experiment. In this comparison the effects of discontinuities in the final mosaic hologram are demonstrated. In both dual lens FINCH systems and the dual lens SAFE system, the same experimental setup has been used. The focal lengths of the two spherical waves were identical in all three experiments. Thus, the properties and the external conditions of the three systems, including focal lengths, temperature, object formation and optical components, were completely identical.

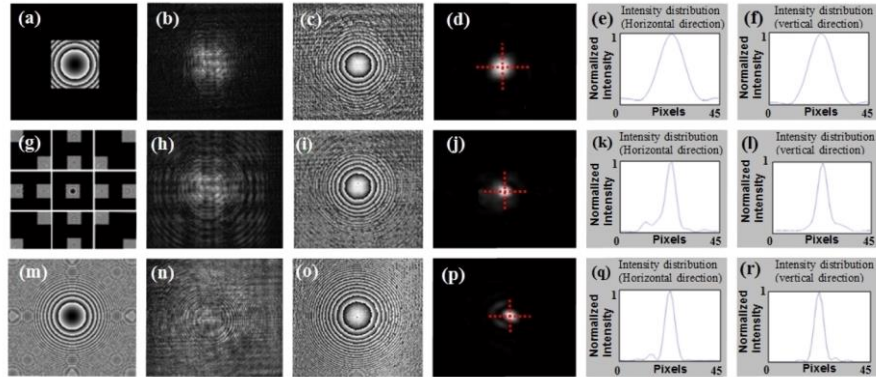


Fig. 4. Experimental results obtained by recording object points with the three systems mentioned in the text: (a) the mask displayed on the SLM in the first dual lens FINCH system (360×360 pixels); (b), (c) the corresponding Fresnel hologram magnitude and phase, respectively; (d) the reconstructed image corresponding to hologram (b), (c); (e), (f) the intensity cross-section of (d) along the horizontal and vertical directions, respectively; (g) the nine masks displayed on the SLM with dual lens SAFE; (h), (i) the corresponding Fresnel hologram magnitude and phase, respectively; (j) the reconstructed image corresponding to hologram (h), (i); (k), (l) the intensity cross-section of (j) along the horizontal and vertical directions, respectively; (m) the mask displayed on the SLM in the second dual lens FINCH system (1080×1080 pixels); (n), (o) the corresponding Fresnel hologram magnitude and phase, respectively; (p) the reconstructed image corresponding to hologram (n), (o); (q), (r) the intensity cross-section of (p) along the horizontal and vertical directions, respectively. The dashed red lines, depicted in (d), (j) and (p), indicate the cross-section paths used in (e), (f), in (k), (l) and in (q), (r).

Figures 4(a), 4(g) and 4(m) show the masks displayed on the SLM for dual lens FINCH consisting of 360×360 pixels, the proposed dual lens SAFE (SA of 1080×1080 pixels) and dual lens FINCH consisting of 1080×1080 pixels, respectively, where the nine combinations of the sub-masks are shown in nine sub squares of Fig. 4(g). In Figs. 4(b) and 4(c), 4(h) and 4(i) and, lastly, 4(n) and 4(o), the magnitude and phase of the holograms of the three compared systems are shown, respectively. In comparison to Fig. 4(b), it is easy to note in Fig. 4(h) that marginal holographic elements were added in the peripheral areas. Moreover, in the hologram phase, additional peripheral information appears around the central area, as is shown in Fig. 4(i), in comparison to Fig. 4(c). However, note in Fig. 4(h) that there are gaps between the various sub-holograms, when compared with Fig. 4(i), which are related to border effects of the nine physical apertures. Figures 4(d), 4(j) and 4(p) show the corresponding reconstructed images of each hologram, computed from Fresnel back propagation. Figures 4(e) and 4(f), 4(k) and 4(l) and, lastly, 4(q) and 4(r) show the intensity cross-section along the horizontal and the vertical axes, with respect to each reconstructed image (Figs. 4(d), 4(j) and 4(p)).

The comparison between the results of the three systems shows a significant narrowing of the SAFE PSF compared with the FINCH PSF with the small physical aperture, as is seen in Figs. 4(k) and 4(l), in comparison with 4(e) and 4(f). This narrowing indicates that SAFE can resolve better than FINCH with the same physical aperture. Furthermore, the experimental results of SAFE are quite similar to those obtained by the equivalent dual lens FINCH (1080×1080 pixels) (comparing Figs. 4(k) and 4(l) and also Figs. 4(q) and 4(r)). However, note that the side-lobes of the PSF of the dual lens SAFE are larger. We believe the side-lobes are larger because of the mentioned gaps between the sub-holograms of the generated mosaic hologram.

3.3 Super resolution experiment

In the second experiment, we recorded a dual lens SAFE hologram of one segment from an RC in order to demonstrate its ability to exceed the resolving power beyond the Rayleigh limit criterion. This experiment was carried out with the same external conditions and system properties as in the PSF experiment described in subsection 3.2. In the RC, the segment of two perpendicular gratings of 18 cycle/mm along both axes was chosen. Although the marginal sub-holograms along the diagonals ($m = \pm 1$ and $n = \pm 1$) do not contribute essential information that can improve the image resolution, i.e., the higher frequencies exist mostly along the Cartesian axes, they were recorded and tiled in order to produce a complete mosaic hologram.

Next, the results of the SAFE experiment are compared with the performance of a conventional imaging system (presented in Fig. 3(c)) and with an equivalent dual lens FINCH system, where both of them are limited by a rectangular aperture of 360×360 pixels. The purpose of this comparison is to evaluate the super-resolution capabilities of the dual lens SAFE system. We also compare the results with those of an equivalent dual lens FINCH system consisting of a rectangular aperture of 1080×1080 pixels (presented in Fig. 3(d)) to analyze the effects of the hologram stitches on the reconstructed image.

According to the Rayleigh criterion, in order to resolve the line pairs on the RC located in the front focal plane of a collimation lens of 400mm focal length with a radiation wavelength of 631nm , the minimal aperture size in a conventional imaging system should be $4.54 \times 4.54\text{mm}$ (567×567 pixels). Therefore, since the aperture size is only 360×360 pixels in the conventional imaging system, the resolving power is not sufficient to resolve all the details in the picture. Figure 5(a) presents the image, produced by the conventional imaging system with three lenses, shown in Fig. 3(c). As is expected, the line grid along both axes is not perceived due to the insufficient physical aperture size of the system. Moreover, in Figs. 5(b), 5(c) the intensities along the horizontal and vertical cross-sections do not indicate the existence of any grating.

In previous studies [14, 15] it was proved and demonstrated that the resolving power of FINCH can be greater than that of a regular incoherent imaging system. Figure 5(d) presents the reconstructed image produced by a 360×360 dual lens FINCH setup. The reconstructed image indeed indicates a significant improvement in the system's resolution; the digits are seen more clearly. However, it is impossible to clearly resolve the 5 lines in the x and y axes. Furthermore, the intensity cross-sections along the horizontal and vertical directions (Figs. 5(e), 5(f)) do not provide any details regarding these lines.

Figure 5(g) presents the reconstructed image of the mosaic hologram created by the proposed dual lens SAFE system. The vertical and horizontal 5 lines are clearly revealed in this figure. A significant improvement occurs in the visibility of these lines shown in Figs. 5(h), 5(i). Moreover, the sharpness of the digits is clearly improved. Figure 5(j) presents the reconstructed image produced by the 1080×1080 dual lens FINCH scheme, where the physical aperture is wide enough to resolve the entire lines. In comparison to Fig. 5(g), the details seem to be smoother. This occurs as a result of the continuity of the produced hologram, contrary to the dual lens SAFE method, which contains the discontinuities in the mosaic hologram. However, the cross-sections along both directions (Figs. 5(k), 5(l)) are similar to those yielded with dual lens SAFE (Figs. 5(e), 5(f)). Thus, we can conclude that, when discussing the resolution properties, in both systems (dual lens SAFE and 1080×1080 dual lens FINCH) the ability to transfer the higher frequencies of an object is similar.

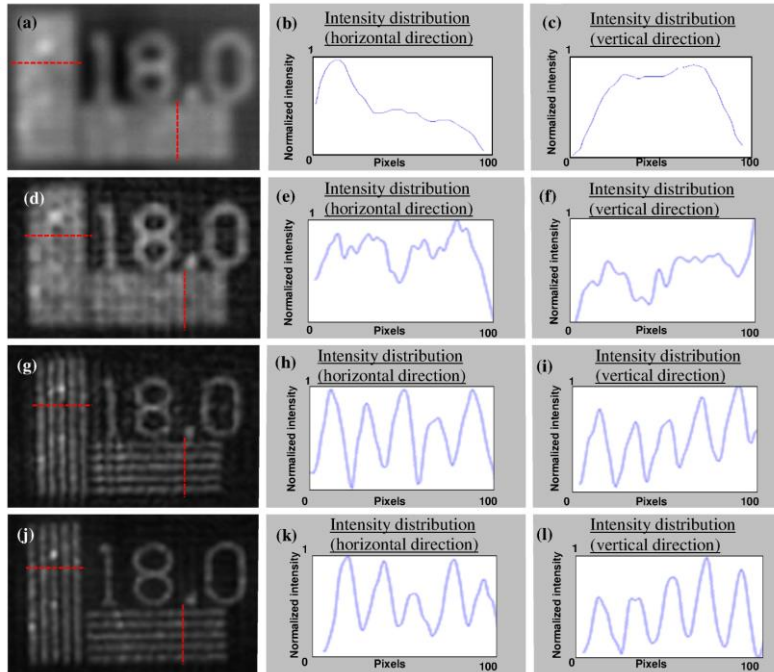


Fig. 5. Experimental results obtained by recording a section of an RC (18 cycle/mm) via the four systems compared in the text: (a) the image obtained by the conventional imaging system; (b), (c) the intensity cross-section of (a) along the horizontal and vertical directions, respectively; (d) the reconstructed image corresponding to the hologram produced by the 360×360 FINCH system; (e), (f) the intensity cross-section of (d) along the horizontal and vertical directions, respectively; (g) the reconstructed image corresponding to the hologram produced by dual lens SAFE; (h), (i) the intensity cross-section of (g) along the horizontal and vertical directions, respectively; (j) the reconstructed image corresponding to the hologram produced by the 1080×1080 FINCH system; (k), (l) the intensity cross-section of (j) along the horizontal and vertical directions, respectively. The dashed red lines, which are depicted in (a), (d), (g) and (j), indicate the path of the cross-sections used in (b), (c), (e), (f), (h), (i), (k) and (l).

3.4. Dual lens SAFE versus T-SAFE

The improvement of the dual lens SAFE compared to other types of SAFE, including T-SAFE [17], is explored experimentally in this section. The influence of the two modifications, i.e. the continuity of the central hologram and the use of dual lens mask displayed on the SLM, are tested separately. The comparative experiment was carried out with the following five different systems:

- Dual lens version of T-SAFE with a stitch in the center ($f_1 = 381.6\text{mm}$ and $f_2 = 945\text{mm}$). [Figs. 6(a-c)]
- T-SAFE with plane and spherical waves ($f_d = z_h/2=271.8\text{mm}$). [Figs. 6(d-f)]
- Dual lens SAFE with two spherical waves ($f_1 = 381.6\text{mm}$ and $f_2 = 945\text{mm}$). [Figs. 6(g-i)]
- SAFE system that established in accordance with the new approach of dual lens SAFE (Fig. 1) with plane and spherical waves ($f_d = z_h/2=271.8\text{mm}$). [Figs. 6(j-l)]
- Dual lens FINCH with two spherical waves ($f_1 = 381.6\text{mm}$ and $f_2 = 945\text{mm}$). [Figs. 6(m-o)]

The five systems have the same effective aperture size, in accordance with the previous experiments ($D_E = 8.64\text{mm}$) and the same setup (positions of the CCD, SLM, glass lenses, etc.) of the previous section (see Fig. 3) was used herein, although the aperture is extended only along the horizontal axis. In order to perform one dimensional SA, in accordance with Ref [17], the object was chosen to be a segment of RC containing only horizontal equally-spaced parallel bars (18 cycle/mm).

Figures 6(a,d,g,j,m) present the masks displayed on the SLM in order to implement the five tested systems, respectively. Figures 6(b,e,h,k,n) present the respective reconstructed images and Figs. 6(c,f,i,l,o) show their cross-sections along the red dashed lines. By comparing Figs. 6(h,i,k,l) and 6(b,c,e,f), it is clearly demonstrated that the reconstructed images created by T-SAFE and its dual lens version are more noisy and with lower visibility, compared to the new approach of SAFE with continuity at the central part of the mosaic hologram. Additionally, when comparing Figs. 6(h,i) and 6(k,l), one can realize that dual lens SAFE is smoother than SAFE with interference of spherical and plane waves. In addition, comparison between the results of the four SA systems to those obtained by dual lens FINCH [Figs. 6(n,o)], yields the conclusion that the results of dual lens SAFE [Fig. 6(h,i)] are the most similar to these of FINCH with the same effective aperture dimensions.

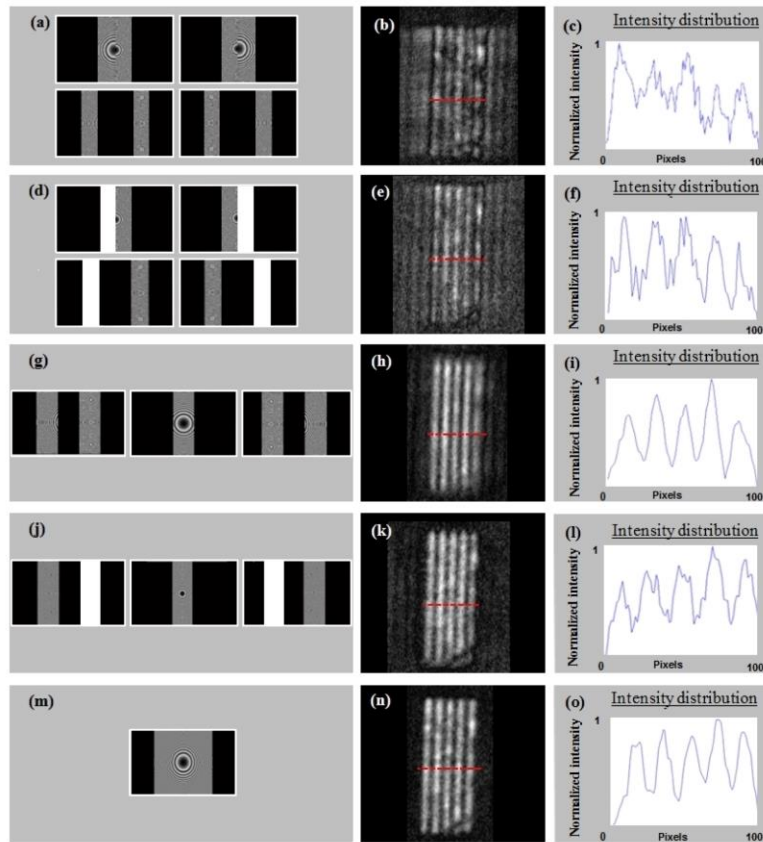


Fig. 6. Experimental results obtained by recording one dimensional equally-spaced parallel bars (18 cycle/mm) by the five systems described in the text: (a) four masks of (270×1080 pixels) displayed on the SLM for dual lens T-SAFE; (b) the reconstructed image of dual lens T-SAFE; (c) the intensity cross-section of (b) along the horizontal direction; (d) four masks of (270×1080 pixels) displayed on the SLM for T-SAFE with plane and spherical waves; (e) the reconstructed image of T-SAFE with plane and spherical waves; (f) the intensity cross-section

of (e) along the horizontal direction; (g) three masks of (360×1080 pixels) displayed on the SLM for dual lens SAFE; (h) the reconstructed image of dual lens SAFE; (i) the intensity cross-section of (h) along the horizontal direction; (j) three masks of (360×1080 pixels) displayed on the SLM for SAFE with plane and spherical waves; (k) the reconstructed image of SAFE with plane and spherical waves; (l) the intensity cross-section of (k) along the horizontal direction; (m) the mask of (1080×1080 pixels) displayed on the SLM for dual lens FINCH; (n) the reconstructed image of dual lens FINCH; (o) the intensity cross-section of (n) along the horizontal direction;

4. Conclusion

We have analyzed the dual lens SAFE system from three different perspectives; first, the PSF of the dual lens SAFE, created by recording a single point source, was compared with the PSF created by equivalent dual lens FINCH systems with the same physical and effective apertures. Second, the reconstruction of an RC recorded by a dual lens SAFE system was compared with the reconstructions of a conventional imaging system and of a dual lens FINCH system with identical physical apertures. Furthermore, we also compared the reconstructed image obtained by the dual lens SAFE system with that obtained from the dual lens FINCH system with the same effective aperture. The process of tiling the sub-holograms to form one big mosaic hologram was based on the algorithm of TPCT.

Third, we compared our proposed SAFE system with T-SAFE system, where both of them were established with dual lens and plan and spherical waves. By this comparison, the importance of the continuity at the central sub-hologram is demonstrated. In addition, the advantage of the dual lens configuration over the setup of plane and spherical waves is validated.

In these three comparative studies the enhanced-resolution capability of the dual lens SAFE system and the improvement of the results over the T-SAFE were demonstrated. Thus, the proposed technique can be used to image any objects without losing details that cannot be resolved by a conventional imaging system with the same physical aperture.

Finally, we should explain the advantage of using SAFE with two channels and two SLMs, as is proposed herein and in Ref [17]. SAFE is actually a composite of several sub-systems which together function as FINCH with a wide synthetic aperture. It has been shown in Ref [14]. that optimal FINCH in sense of maximum resolution is obtained when there is a complete overlap between the interfering waves on the camera plane for each object point. A complete overlap is obtained if and only if, for each camera patch, besides the central patch, the interfering waves are coming from two sides of the optical axis. FINCH is composed from several sub-systems of SAFE, where each of which is responsible to a single camera patch. Therefore, besides the central patch, all the other interference patches are created from waves coming from two different sides of the optical axis. In other words the two waves come through two separated optical channels. Can the technique of SAFE be carried out using only a single optical channel? The answer is yes, but in a cost of a significant reduction of the overall image resolution that can be achieved by the complete system. To conclude, in order to maximize the resolution that can be obtained from SAFE with a given synthetic aperture, the system should be operated in a configuration of two separated channels.

Acknowledgments

This work was supported by The Israel Ministry of Science and Technology (MOST); The Israel Science Foundation (ISF) (Grant No. 439/12); National Institutes of Health (NIH) (U54GM105814)